Smart Mater. Struct. 6 (1997) 106–116. Printed in the UK

PII: S0964-1726(97)79230-9

Feasibility analysis of using piezoceramic transducers for cantilever beam modal testing*

Bor-Tsuen Wang and Chung-Chei Wang

Department of Mechanical Engineering, National Pingtung Polytechnic Institute, Pingtung, Taiwan 91207, Republic of China

Received 15 April 1996, accepted for publication 18 October 1996

Abstract. This paper presents a theoretical analysis of the application of piezoceramic transducers to cantilever beam modal testing. Four pairs of sensors and actuators, including accelerometer–point force, accelerometer–PZT, PVDF–point force and PVDF–PZT, are considered. The frequency response functions (FRFs) for the four pairs of sensors and actuators are first derived and written in the conventional modal format. The characteristics of modal parameters can thus be interpreted through the FRFs. A column of the FRF matrix can then be obtained based on the theoretical formulation. A curve-fitting algorithm is then applied to extract the modal parameters, such as natural frequencies, mode shapes and damping ratios. Results show that any sensor–actuator pair can successfully determine natural frequencies and damping ratios. Point types of transducer result in the displacement mode shapes, while piezoceramic transducers that are strip types and distributed in sense give the mode shapes of the slope difference between the edges of piezoceramic transducers. The paper provides the theoretical basis of applying piezoceramic transducers to experimental modal analysis and numerically supports the feasibility of cantilever beam modal testing using piezoceramic transducers.

1. Introduction

Experimental modal analysis has been shown to be an effective means of studying of structural dynamic characteristics. The mobility measurement is essential to obtain a set of frequency response functions (FRFs). Either the shaker or impact hammer is conventionally used as the excitor, while the accelerometer serves as the response measurement device [1–6]. A scanning laser Doppler vibrometer can also be applied for non-contact measurement and has been shown to be effective to obtain modal properties, such as natural frequencies, mode shapes and damping ratios [7, 8].

Piezoceramic transducers have been widely used in active vibration and acoustic control [9–12]. Many researchers have developed analytical models for the characterization of PZT actuators in pure bending [13–16] and asymmetric [17, 18] excitation. PVDF (polyvinylidene fluoride) has also been successfully used as error sensors for structural vibration and acoustic control [19, 20]. The mathematical models of piezoceramic transducers are well developed and experimentally verified for simple structure applications such as a beam [13, 14, 16, 21], plate [15, 22] or cylinder [23]. The piezoceramic transducers have unique advantages over the conventional transducers, such as low weight and low cost. The most important can be that they are distributed in sense and can be integrated into structures without affecting structure properties. The so called intelligent materials structures and systems (IMSSs) have been applied to active control systems. The ideas of IMSSs can also be applied to structural testing and fault diagnosis. Therefore, the use of piezoceramic transducers for structural testing is also of interest. Sun *et al* [24] measured the electric admittance of PZT actuators incorporated with the use of accelerometers and derived their frequency response functions to study dynamic properties of a beam. Cole *et al* [25] performed the modal testing of piezostructures and obtained the electromechanical coupling (EMC) matrices to characterize the pole-residue properties. Both works induce the idea of structural testing by using piezoceramic transducers, but they did not properly recognize the nature of piezostructures.

This paper presents the theoretical basis of the use of piezoceramic transducers for structural modal testing. A cantilever beam is considered as the test structure. Piezoceramic transducers, such as PZT actuators and PVDF sensors, are used as the input and output measurement devices, and conventional transducers, such as shakers (point force) and accelerometers, are also presented for

* Partial results of this paper were presented at the *12th National Conference of the Chinese Society of Mechanical Engineers (Chia-Yi, 1995).*

0964-1726/97/010106+11$19.50

the purpose of comparison. Four pairs of actuator and sensor combinations, i.e., accelerometer–point force, accelerometer–PZT, PVDF–point force and PVDF–PZT, are considered. The theoretical FRFs are first derived and written in conventional modal format; therefore, the physical characteristics of modal parameters can be well recognized. The displacement mode shapes and the slope difference mode shapes are identified for point types of conventional transducer and distributed types of piezoceramic transducer respectively. The synthetic modal analysis that directly uses the theoretical FRFs for modal parameter extraction or curve fitting is then performed. The modal parameters, including natural frequencies, damping ratios and mode shapes of the cantilever beam, can be successfully obtained. This work enhances the feasibility of intelligent structural modal testing (ISMT) and the possibility of remote structural modal testing (RSMT).

2. Theoretical analysis

2.1. Free vibration analysis

Consider a thin uniform cantilever beam with length L_b as shown in figure 1. By neglecting the effect of shear deformation and rotary inertia, the governing equation of the beam can be obtained as follows:

$$E_b I_b \frac{\partial^4 y(x,t)}{\partial x^4} + \rho_b b_b t_b \frac{\partial^2 y(x,t)}{\partial t^2} = p(x,\ t) \tag{1}$$

in which y is the transverse displacement; E_b is Young's modulus; I_b is the moment of inertia; ρ_b is the beam density; b_b is the beam width; t_b is the beam thickness; $p(x,\ t)$ is the force function. The subscript b thus denotes the beam.

The boundary conditions of a cantilever beam are fixed at one end and free at the other. If $x = 0$ is the fixed end, the displacement and slope are to be zero.

$$y(x = 0,\ t) = \left.\frac{\partial y(x,t)}{\partial x}\right|_{x=0} = 0. \tag{2}$$

If the free end is at $x = L_b$, the bending moment and shear force are then zero.

$$\left.E_b I_b \frac{\partial^2 y(x,t)}{\partial x^2}\right|_{x=L_b} = \left.\frac{\partial}{\partial x}\left(E_b I_b \frac{\partial^2 y(x,t)}{\partial x^2}\right)\right|_{x=L_b} = 0. \tag{3}$$

Let $y(x,t) = \phi(x)q(t)$ substitute into equation (1). By using the method of separation of variables and applying the boundary conditions, one can obtain the characteristic equation [26] as follows:

$$1 + \cos \alpha_n L_b \cosh \alpha_n L_b = 0. \tag{4}$$

The characteristic values α_n ($n = 1, 2, \ldots$) can then be solved numerically as follows:

$$\begin{aligned} \alpha_1 L_b &= 1.875104 \\ \alpha_2 L_b &= 4.694091 \\ \alpha_3 L_b &= 7.854757 \\ &\vdots \end{aligned} \tag{5}$$

The natural frequencies can then be determined [26]

$$\omega_n = (\alpha_n L_b)^2 \sqrt{\frac{E_b I_b}{\rho_b b_b t_b L_b^4}} = \alpha_n^2 \sqrt{\frac{E_b I_b}{\rho_b b_b t_b}} \tag{6}$$

and the corresponding mode shape functions are identified as follows:

$$\phi_n(x) = \cosh \alpha_n x - \cos \alpha_n x = \sigma_n(\sinh \alpha_n x - \sin \alpha_n x) \tag{7}$$

where

$$\sigma_n = \frac{\sinh \alpha_n L_b - \sin \alpha_n L_b}{\cosh \alpha_n L_b + \cos \alpha_n L_b}. \tag{8}$$

It is noted that $\phi_n(x)$ is a continuous function and represents the displacement.

2.2. Forced vibration analysis

2.2.1. Point force excitation. Consider the jth harmonic point force acting at $x = x_{F_j}$ as shown in figure 1. The external force function can be expressed as follows:

$$p(x,\ t) = F_j \delta(x - x_{f_j}) e^{i\omega t} \tag{9}$$

in which F_j is the magnitude of the jth point force; $\delta(x)$ is the Dirac delta function; x_{f_j} is the location of the jth point force. The system response is also harmonic. From the expansion theorem, the system response can be assumed:

$$y(x,\ t) = e^{i\omega t} \sum_{n=1}^{\infty} W_n \phi_n(x) \tag{10}$$

where W_n and $\phi_n(x)$ are the modal amplitude and mode shape function respectively. By substituting equation (10) into equation (1), pre-multiplying by $\phi_m(x)$ and integrating over the beam length, the governing equation can be simplified with the use of orthogonality properties of the mode shape function; therefore, the modal amplitude can be obtained:

$$W_n = \frac{\frac{1}{L_b} F_j \phi_n(x_{f_j})}{E_b I_b \alpha_n^4 - \rho_b b_b t_b \omega^2} = \frac{\frac{1}{L_b} F_j \phi_n(x_{f_j})}{\rho_b b_b t_b (\omega_n^2 - \omega^2)}. \tag{11}$$

The displacement response can then be written as follows:

$$y(x,\ t) = e^{i\omega t} \sum_{n=1}^{\infty} \frac{\frac{1}{L_b} F_j \phi_n(x_{f_j}) \phi_n(x)}{\rho_b b_b t_b (\omega_n^2 - \omega^2)}. \tag{12}$$

If the ith accelerometer is chosen to be the output measurement device, and the jth point force is applied as the actuation force as shown in figure 1, the FRF between the acceleration amplitude of the ith accelerometer and the magnitude of the jth point force can be shown as follows:

$$\alpha_{a_i F_j}(\omega) = \frac{\ddot{y}_i}{F_j} = -\omega^2 \sum_{n=1}^{\infty} \frac{\frac{1}{L_b} \phi_n(x_{f_j}) \phi_n(x_{a_i})}{\rho_b b_b t_b (\omega_n^2 - \omega^2)} \tag{13}$$

where x_{a_i} is the location of the ith accelerometer.

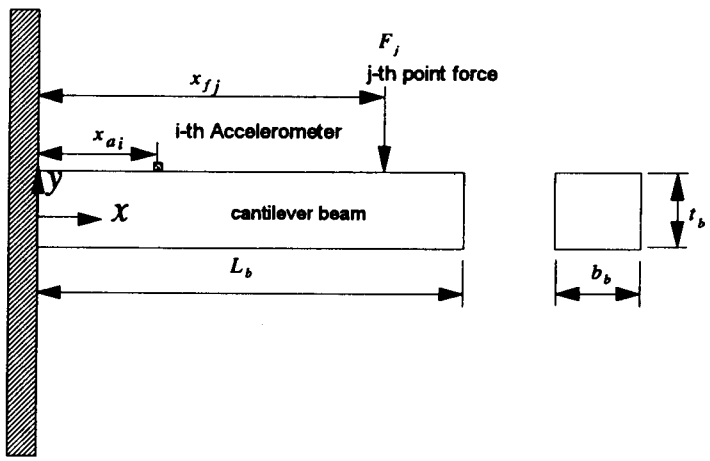

Figure 1. The conventional transducers on the cantilever beam.

2.2.2. PZT pure bending excitation. Consider the jth PZT patches to be symmetrically bonded on the top and the bottom of the beam and applied voltage V_{c_j} 180° out of phase as shown in figure 2. The equivalent force induced by the PZT patches can be shown as two concentrated moments at both edges of the PZT patches [16], and therefore the force function can be expressed as follows:

$$p(x, t) = M_{eq}\left[\delta'(x - x_{c1_j}) - \delta'(x - x_{c2_j})\right] e^{i\omega t} \tag{14}$$

where x_{c1_j} and x_{c2_j} are the location coordinates of the jth PZT actuator; M_{eq} is the equivalent moment induced by the PZT actuator and represented by the first derivative of the Dirac delta function. M_{eq} is given by

$$M_{eq} = C_0 \Lambda \tag{15}$$

$$\Lambda = \frac{d_{31}}{t_c} V_{c_j} \tag{16}$$

$$C_0 = \frac{t_b^2 E_b}{6 + \Psi} b_c \tag{17}$$

$$\Psi = \frac{t_b E_b}{t_c E_c} \tag{18}$$

where Λ is the free strain of the PZT patches induced by the voltage; Ψ is the effective stiffness ratio; V_{c_j} is the applied voltage; d_{31} is the piezoelectric dielectric strain constant; E_c Young's modulus of the PZT patch; b_c and t_c are the width and thickness of the PZT patch respectively. The subscript c denotes the PZT actuator.

Similar to the point force excitation, the frequency response function between the acceleration amplitude of the ith accelerometer and the applied voltage to the jth PZT actuator can be derived as follows:

$$\alpha_{a_i c_j}(\omega) = \frac{\ddot{y}_i}{V_{c_j}} = -\omega^2 \sum_{n=1}^{\infty} \frac{\frac{1}{L_b}\frac{C_0 d_{31}}{t_c}[\phi_n'(x_{c2_j}) - \phi_n'(x_{c1_j})]\phi_n(x_{a_i})}{\rho_b b_b t_b(\omega_n^2 - \omega^2)}. \tag{19}$$

2.3. PVDF sensing approach

A strip of PVDF patch can also be applied as the sensing device as shown in figure 2. The shape function of the ith PVDF sensor can be expressed as follows:

$$\Gamma(x) = u(x - x_{p1_i}) - u(x - x_{p2_i}) \tag{20}$$

where x_{p1_i} and x_{p2_i} are the location coordinates of the ith PVDF sensor; $u(x)$ is the unit step function. The subscript p indicates the PVDF sensor. The sensing equation of the PVDF sensor is [27]

$$q(t) = \frac{(t_b + t_p)}{2} b_p e_{31} \int_0^{L_b} \Gamma(x) \frac{\partial^2 y(x, t)}{\partial x^2} \, dx \tag{21}$$

where $q(t)$ is the charge; t_p and b_p are the thickness and width of the PVDF sensor respectively; e_{31} is the piezoelectric field intensity constant. The resultant voltage can be written

$$V_{p_i}(t) = \frac{q(t)}{\varepsilon A_p} t_p \tag{22}$$

where $V_{p_i}(t)$ is the measured voltage; ε is the permittivity; A_p is the area of the PVDF sensor, i.e., $A_p = b_p l_p$. The ith PVDF voltage can be rewritten as

$$V_{p_i}(t) = \frac{t_p}{\varepsilon A_p} \frac{(t_b + t_p)}{2} b_p e_{31} e^{i\omega t} \sum_{n=1}^{\infty} W_n \left[\phi_n'(x_{p2_i})\phi_n'(x_{p1_i})\right]. \tag{23}$$

If the ith PVDF sensor is used as the output sensing device, and the jth point force is applied as the input force, the FRF between the measured voltage of the ith PVDF sensor and the force amplitude of the jth force can be derived as follows:

$$\alpha_{p_i F_j} = \frac{V_{p_i}}{F_j} = \frac{t_p}{\varepsilon A_p} \frac{(t_b + t_p)}{2} b_p e_{31} \sum_{n=1}^{\infty} \frac{\frac{1}{L_b}\phi_n(x_{f_j})[\phi_n'(x_{p2_i}) - \phi_n'(x_{p1_i})]}{\rho_b b_b t_b(\omega_n^2 - \omega^2)}. \tag{24}$$

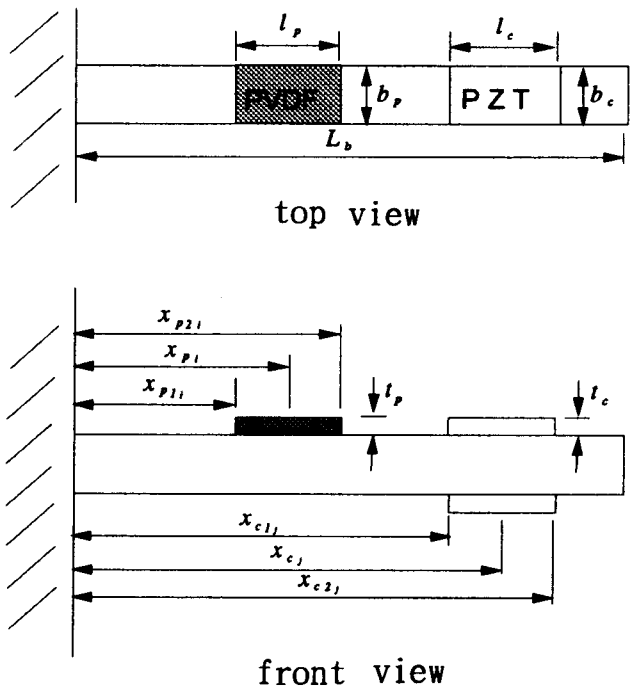

Figure 2. The piezoceramic transducers on the cantilever beam.

Similarly, the FRF between the measured voltage of the ith PVDF sensor and the voltage amplitude applied by the PZT actuator can be obtained as follows:

$$\alpha_{p_i c_j} = \frac{V_{p_i}}{V_{c_j}} = \frac{t_p}{\varepsilon A_p}\frac{(t_b + t_p)}{2} b_p e_{31} \sum_{n=1}^{\infty} \times \frac{\frac{1}{L_b}\frac{C_0 d_{31}}{t_c}[\phi_n'(x_{c2_j}) - \phi_n'(x_{c1_j})][\phi_n'(x_{p2_i}) - \phi_n'(x_{p1_i})]}{\rho_b b_b t_b(\omega_n^2 - \omega^2)}. \tag{25}$$

2.4. Frequency response functions

Subsections 2.2 and 2.3 respectively derived the FRFs for four pairs of actuators and sensors, including (i) accelerometer–point force, (ii) accelerometer–PZT actuator, (iii) PVDF sensor–point force and (iv) PVDF sensor–PZT actuator. If we let x_{c_j} be the central location of the jth PZT actuator and x_{p_i} be the central location of the ith PVDF sensor as shown in figure 2, then $x_{c1_j} = x_{c_j} - l_c/2$, $x_{c2_j} = x_{c_j} + l_c/2$, $x_{p1_i} = x_{p_i} - l_p/2$, $x_{p2_i} = x_{p_i} + l_p/2$. If the viscously damped model is considered, the FRFs can be summarized as follows:

$$\alpha_{a_i F_j} = \frac{\ddot{y}_{a_i}}{F_j} = -\omega^2 \sum_{n=1}^{\infty} \frac{{}_i\Phi_{nj}^a \Phi_n^f}{\rho_b b_b t_b[(\omega_n^2 - \omega^2) + \mathrm{i}2\zeta_n\omega_n\omega]} \tag{26}$$

$$\alpha_{a_i c_j} = \frac{\ddot{y}_{a_i}}{V_{c_j}} = -\omega^2 \sum_{n=1}^{\infty} \frac{{}_i\Phi_{nj}^a \Phi_n^c}{\rho_b b_b t_b[(\omega_n^2 - \omega^2) + \mathrm{i}2\zeta_n\omega_n\omega]} \tag{27}$$

$$\alpha_{p_i F_j} = \frac{V_{p_i}}{F_j} = -\omega^2 \sum_{n=1}^{\infty} \frac{{}_i\Phi_{nj}^p \Phi_n^f}{\rho_b b_b t_b[(\omega_n^2 - \omega^2) + \mathrm{i}2\zeta_n\omega_n\omega]} \tag{28}$$

$$\alpha_{p_i c_j} = \frac{V_{p_i}}{V_{c_j}} = -\omega^2 \sum_{n=1}^{\infty} \frac{{}_i\Phi_{nj}^p \Phi_n^c}{\rho_b b_b t_b[(\omega_n^2 - \omega^2) = \mathrm{i}2\zeta_n\omega_n\omega]} \tag{29}$$

where

$${}_i\Phi_n^a = \sqrt{\frac{1}{L_b}}\phi_n(x_{a_i}) \tag{30}$$

$${}_j\Phi_n^f = \sqrt{\frac{1}{L_b}}\phi_n(x_{f_j}) \tag{31}$$

$${}_i\Phi_n^p = \sqrt{\frac{1}{L_b}} k_p\left[\phi_n'(x_{p_i} + l_p/2) - \phi_n'(x_{p_i} - l_p/2)\right]$$

$$k_p = \frac{t_p}{\varepsilon A_p}\frac{t_b + t_p}{2} b_p e_{31} \tag{32}$$

$${}_j\Phi_n^c = \sqrt{\frac{1}{L_b}} k_c\left[\phi_n'(x_{c_j} + l_c/2) - \phi_n'(x_{c_j} - l_c/2)\right]$$

$$k_c = \frac{C_0 d_{31}}{t_c} \tag{33}$$

$$\phi_n'(x) = \alpha_n[\sinh\alpha_n x + \sin\alpha_n x - \sigma_n(\cosh\alpha_n x - \cos\alpha_n x)]. \tag{34}$$

${}_i\Phi_n^a$ and ${}_j\Phi_n^f$ represent the values of the nth acceleration and point force mode shape functions at the ith and jth locations of the accelerometer and point force respectively. ${}_i\Phi_n^p$ and ${}_j\Phi_n^c$ represent the values of the nth PVDF and PZT mode shape functions at the ith and jth location of the PVDF sensor and PZT actuator respectively. The PVDF and PZT mode shape functions are proportional to the mode shape of the slope difference between the two edges of PVDF and PZT patches, while the accelerometer and point force mode shape functions are proportional to the displacement mode shape function. Generally speaking, the displacement mode shape has orthogonality properties; however, the slope difference mode shape has not. Wang

[28] demonstrated that the slope difference mode shape is proportional to the displacement mode shape for a simply supported beam. Here, for a cantilever beam the slope difference mode shape is not proportional to the displacement mode shape. The characteristics of the mode shapes and their relationships will be further discussed.

It should be noted that in practical measurement a continuous structure is always discretized, and so only a finite number of points N can be measured. The $N \times N$ FRF matrix can then be measured through the mobility measurement. The FRF matrix $[\alpha_{ij}]$ can be defined as follows:

$$\{Z_i\}_{N\times 1} = [\alpha_{ij}]_{N\times N}\{P_j\}_{N\times 1} \tag{35}$$

where $\{Z_i\}_{N\times 1}$ and $\{P_j\}_{N\times 1}$ represent the output and input vectors respectively. The components of the FRF matrix are shown in equations (26)–(29), which are written in the conventional FRF format. From observation of equations (26)–(29), the main difference of the FRFs is the numerator, that is the residue, also called the modal constant. The modal constant is the product of the sensor and actuator mode shape components. It is also noted that the mode shape function is usually approximated by the $N \times 1$ mode shape vector. Therefore, ${}_i\Phi_n^a$, ${}_j\Phi_n^f$, ${}_i\Phi_n^p$ and ${}_j\Phi_n^c$ can also denote the ith or jth component of the accelerometer, point force actuator, PVDF sensor and PZT actuator mode shape vectors respectively.

To perform experimental modal analysis, at least, either a row or a column of the FRF matrix must be measured. By roving the actuator, a row of the FRF matrix can be obtained; by roving the sensor, a column of the FRF matrix will be obtained. For the conventional experimental modal testing, the point force and accelerometer are usually used as the actuator and sensor. Their FRF is shown in equation (26). Both ${}_i\Phi_n^a$ and ${}_j\Phi_n^f$ for the modal constant are associated with displacement mode shapes; therefore, roving either actuator or sensor, the displacement mode shapes can always be extracted from the curve-fitting procedures.

If the accelerometer is used as the sensor, and the PZT patches are applied as the actuator, then the FRF is shown in equation (27). When the accelerometer is fixed, and the PZT actuator is roving, a row of the FRF matrix will be obtained. The PZT actuator mode shape that is the slope difference mode shape will be extracted by performing curve-fitting procedures on the FRFs. Conversely, when the PZT actuator is fixed, and the accelerometer is roving, then a column of the FRF matrix will be obtained. The accelerometer mode shape that is the displacement mode shape can then be extracted. For other pairs of combinations of actuators and sensors, the physical meaning of the extracted mode shapes with respect to the testing procedure is summarized in table 1. In summary, when the sensor is roving with the actuator fixed during testing, a column of the FRF matrix can be determined. The extracted mode shape will then be characterized by the sensor mode shape. Conversely, when the actuator is roving with the sensor fixed, a row of the FRF matrix can be obtained. The extracted mode shape will then be characterized by the actuator mode shape.

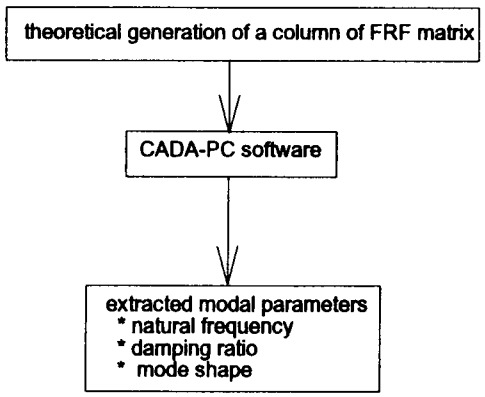

Figure 3. A flow chart for synthetic modal analysis.

3. Synthetic modal analysis

The normal procedure of experimental modal analysis includes the measurement of FRFs and the data analysis of FRFs, so called curve fitting or extraction of modal parameters. The measurement of FRFs depends on the types of actuation and sensing device. The data analysis of FRFs is to extract the modal parameters, including natural frequencies, damping ratios and mode shapes, from the measured FRFs. This work obtains the FRFs based on the theoretical formulation as shown in section 2 instead of practical measurement. By assuming a roving sensor, a column of the FRF matrix can be theoretically determined for the four sensor–actuator pair approaches. The modal parameter estimation is conducted by using the MDOF curve-fitting algorithm provided by CADA-PC software [29]. The least-squares complex exponential (LSCE) method is applied to obtain the poles of FRFs, i.e., the natural frequencies, and the least-squares frequency domain (LSFD) method is used to determine the residues. The synthetic modal analysis procedure is illustrated in figure 3 and can be applied to show the feasibility of using piezoceramic transducers for experimental modal testing of a cantilever beam.

4. Results and discussion

Consider a steel beam with properties as shown in table 2 for numerical simulation. The first ten natural frequencies were calculated and are listed in table 3. The beam is equally divided into 15 divisions and numbered in sequence as shown in figure 4. The point force and accelerometer are assumed to be applied at the dots shown in figure 4. The PZT (G-1195 [30]) and PVDF (DT1-028K [31]) patches with material properties as shown in table 4 are assumed to be 20 mm in length, and of the same width as the beam. The PZT actuators and PVDF sensors can then be applied at each position illustrated in figure 4. In the simulation, the viscous damping ratios for all modes are assumed to be 0.01. A total number of 15 modes is included for obtaining the theoretical FRFs. The FRFs are then used for performing modal parameter estimation with the methods

Table 1. Physical meanings of mode shapes with respect to test procedure.

Sensor	Actuator	Roving actuator with fixed sensor (a row of FRF matrix)	Roving sensor with fixed actuator (a column of FRF matrix)
accelerometer	point force	displacement mode shape	displacement mode shape
accelerometer	PZT	slope difference mode shape	displacement mode shape
PVDF	point force	displacement mode shape	slope difference mode shape
PVDF	PZT	slope difference mode shape	slope difference mode shape

Table 2. Physical properties of the cantilever beam.

Materials	Steel
Length (L_b)	0.3 m
Width (b_b)	0.04 m
Thickness (t_b)	0.002 m
Density (ρ_b)	7870 kg m^{-3}
Young's modulus (E_b)	207 ± 10^9 N m^{-2}

Table 3. Theoretical natural frequencies of the first ten modes.

Mode	Natural frequency (Hz)
1	18.411
2	115.377
3	323.058
4	633.064
5	1046.501
6	1563.291
7	2183.440
8	2906.946
9	3733.812
10	4664.034

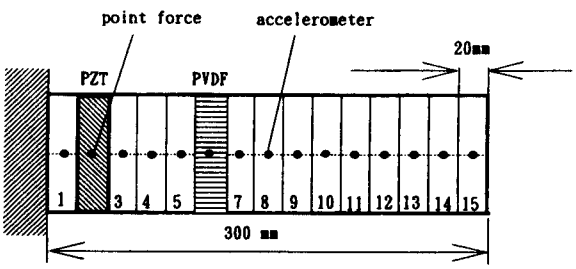

Figure 4. The division of the cantilever beam.

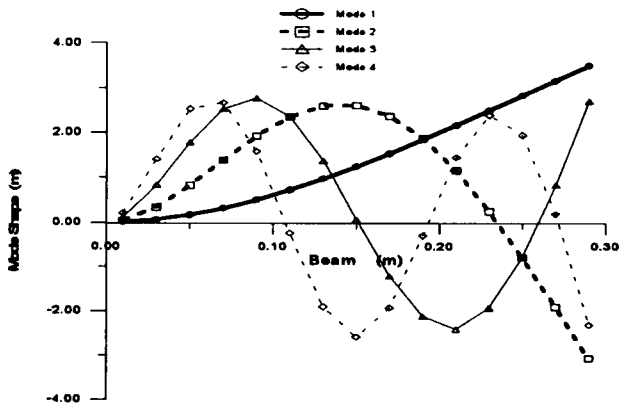

Figure 5. The theoretical mode shapes of the conventional transducers.

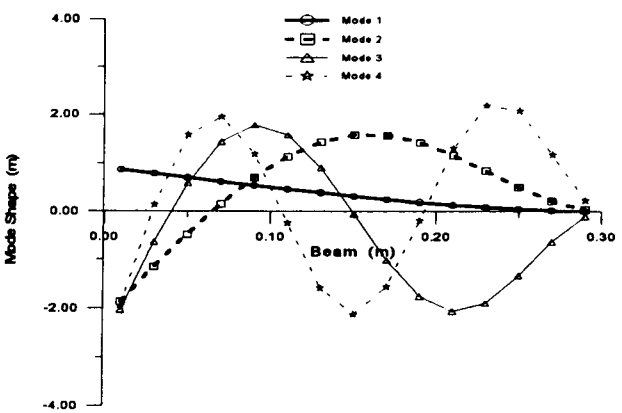

Figure 6. The theoretical mode shapes of the piezoceramic transducers.

described in the previous section. The companion paper [32] by the present authors has presented the verification of experimental results.

4.1. Theoretical mode shapes

The mode shapes of accelerometer and point force as shown in equations (30) and (31) are displacement mode shapes. The first four mode shapes of the conventional transducers are shown in figure 5. The PZT and PVDF mode shapes as shown in equations (32) and (33) are proportional to the slope difference between two edges of piezoceramic transducers. The first four mode shapes of the piezoceramic transducers are shown in figure 6. The piezoceramic transducer mode shapes can be observed as the mirror image of the conventional transducer mode shapes against the wall for the case of the cantilever beam. In general, the conventional transducer mode shapes for accelerometer and point force are displacement mode shapes, while the piezoceramic transducer mode shapes are the mode shapes of the slope difference between two edges of the piezoceramic patches.

4.2. Generation of the theoretical FRFs

The simulation assumes that the actuation forces including point force and PZT excitation are applied at position

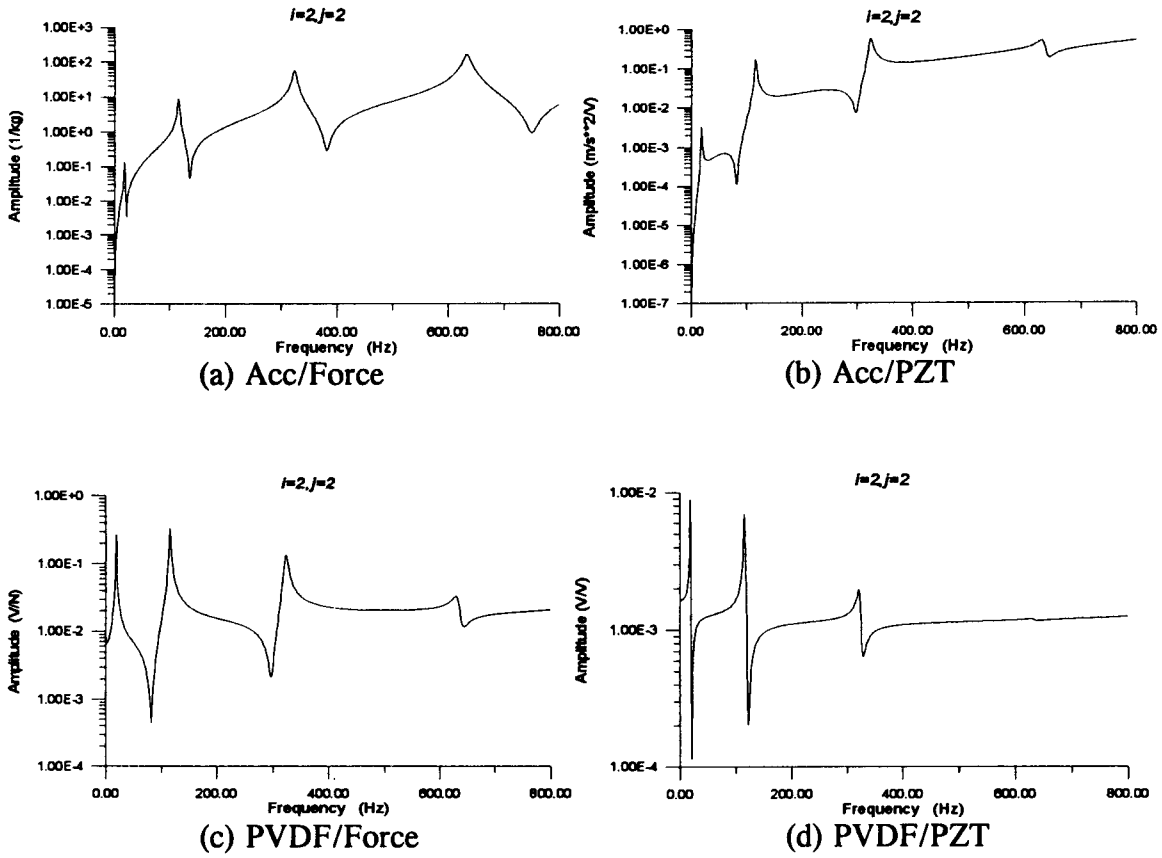

Figure 7. Theoretical point frequency response functions for $i = 2$ and $j = 2$.

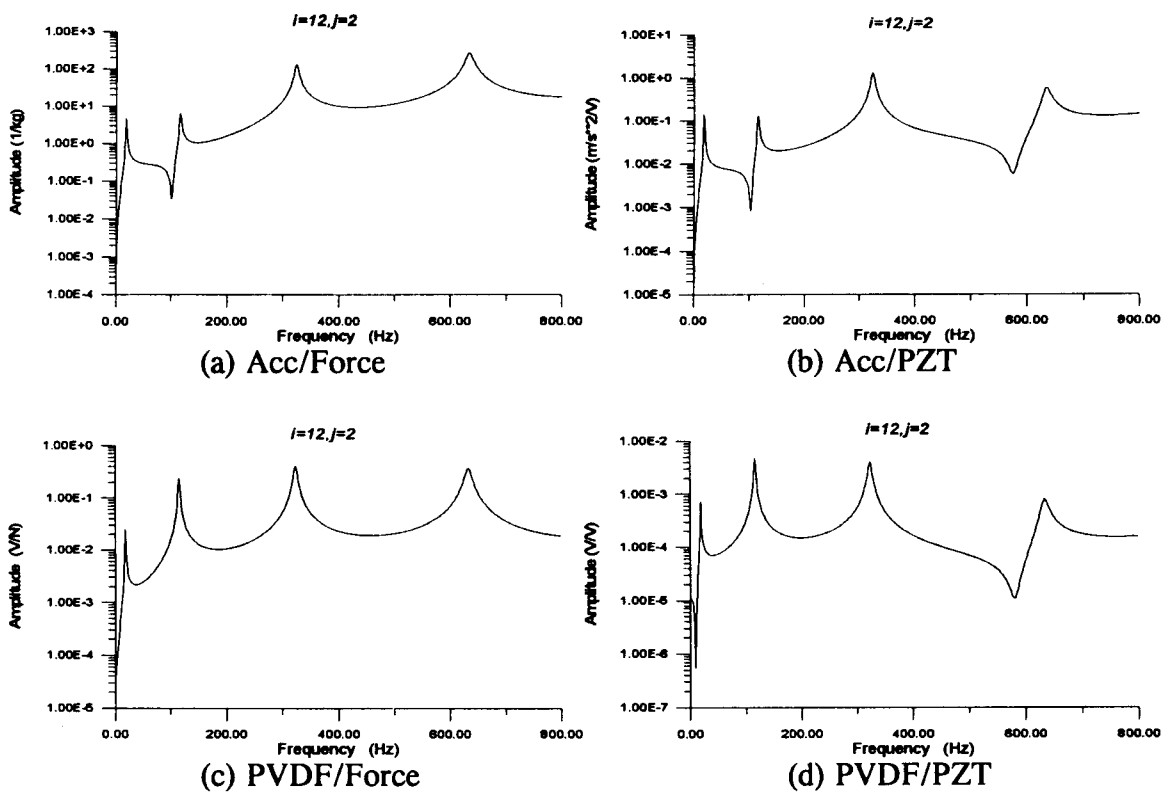

Figure 8. Theoretical transfer frequency response functions for $i = 12$ and $j = 2$.

Table 4. Piezoceramic material properties.

PZT actuator (G-1195) [30]	PVDF sensor (DT1-028K) [31]
$E_c = 6.3 \times 10^{10}$ N m^{-2}	$E_p = 2 \times 10^9$ N m^{-2}
$\rho_c = 7650$ kg m^{-3}	$\rho_p = 1800$ kg m^{-3}
$\nu_c = 0.28$	$\nu_p = 0.33$
$d_{31} = d_{32} = 166 \times 10^{-12}$ m V^{-1}	$e_{31} = 54 \times 10^{-3}$ C m^{-1}
$t_c = 1.905$ mm	$t_p = 28 \times 10^{-6}$ m
	$\varepsilon = 106 \times 10^{-12}$ F m^{-1}

$j = 2$ respectively. The accelerometer is roving from position 1 to 15. For PVDF sensor application, only the even-number positions are applied. The analysis frequency range is between 0 and 800 Hz. A total number of 1024 data points for each FRF in the frequency range is generated for the curve-fitting process. The point FRFs, i.e., where the response measurements and driving points coincide, for $i = 2$ and $j = 2$ are shown in figure 7(a)–(d). One can see that anti-resonance points occur between all resonance points. The transfer FRFs, i.e., where the response measurements and driving points are different, for $i = 12$ and $j = 2$ as shown in figure 8(a)–(d) are to demonstrate the characteristics of transfer FRFs. The anti-resonance points do not always appear between resonance points.

4.3. Synthetic modal analysis

The generated FRFs for each actuator–sensor pair approach can be further analyzed by using MDOF curve-fitting algorithms provided by CADA-PC software. The modal parameters including natural frequencies, damping ratios and mode shapes can then be obtained. The following shows the comparison and discussion of the synthesized results.

Table 5 shows the comparison of natural frequencies derived from the theoretical analysis and from the synthetic modal analysis for the four actuator–sensor pair approaches. The error percentage with respect to the theoretical model is also indicated in parenthesis. As expected, the results for the conventional transducer pair (Acc–Force) agree very well with the theoretical natural frequencies. The synthetic modal analysis (SMA) is then considered sufficiently accurate. When the piezoceramic transducers are applied, the natural frequencies can also be accurately predicted except the first natural frequency, that has about 5% discrepancy. The discrepancy may be due to the frequency resolution of FRFs. Nevertheless, either actuator–sensor pair approach can satisfactorily predict the system natural frequencies.

Table 6 shows the comparison of viscous damping ratio derived from the synthetic modal analysis and the theoretical model assumptions. One can see that there is no more than 5% difference in comparison to the theoretical assumption of modal damping ratio 0.01 for each mode. In particular, for the applications of piezoceramic transducers, the prediction of damping ratio is less than 2% in comparison to the theoretically assumed modal damping ratio. It is noted that in practical applications

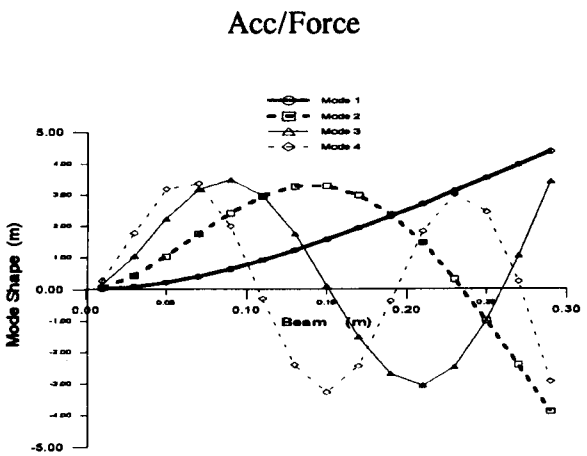

Figure 9. The prediction of the mode shapes from SMA for Acc–Force.

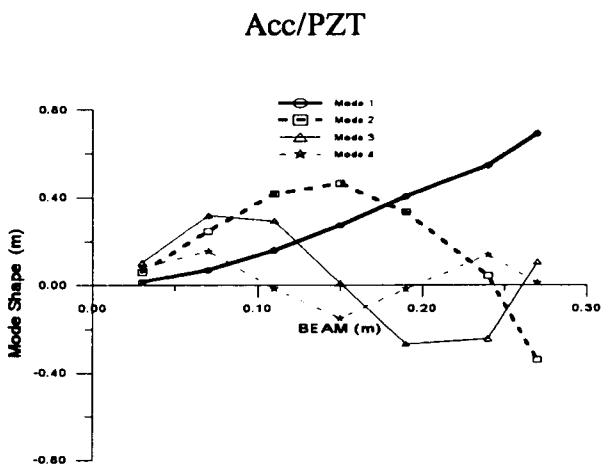

Figure 10. The prediction of the mode shapes from SMA for Acc–PZT.

of piezoceramic transducers the damping effect due to the piezoceramic patches and glue effects, which are not treated in this work, may not be neglected.

Figure 9 shows the first four mode shapes extracted from the synthetic modal analysis for the accelerometer and point force pair. As expected, the mode shape is just the displacement mode shape and agrees well with those shown in figure 5. Figure 10 shows the first four mode shapes derived from the accelerometer and PZT actuator pair. The mode shapes are not so smooth as those shown

Table 5. A comparison of natural frequencies between theoretical analysis and synthetic modal analysis (SMA).

	First natural frequency	Second natural frequency	Third natural frequency	Fourth natural frequency
Theoretical analysis	18.411	115.377	323.058	633.064
SMA for Acc–Force	18.422 (0.062%)	115.372 (−0.044%)	323.041 (−0.053%)	632.938 (−0.019%)
SMA for Acc–PZT	17.411 (−5.429%)	114.371 (−0.872%)	322.057 (−0.310%)	632.031 (−0.872%)
SMA for PVDF–Force	17.420 (−5.383%)	114.371 (−0.872%)	323.063 (−0.022%)	632.031 (−0.163%)
SMA for PVDF–PZT	17.406 (−5.495%)	114.373 (−0.870%)	323.043 (−0.005%)	632.028 (−0.164%)

Table 6. Comparison of modal damping ratio (%) between theoretical analysis and SMA.

Mode	Theoretical analysis (assumed)	SMA for Acc–Force	SMA for Acc–PZT	SMA for PVDF–Force	SMA for PVDF–PZT
1	1.00	0.95	1.04	1.03	1.01
2	1.00	1.00	1.01	1.01	1.01
3	1.00	1.00	1.00	1.01	1.00
4	1.00	1.01	1.01	1.02	1.01

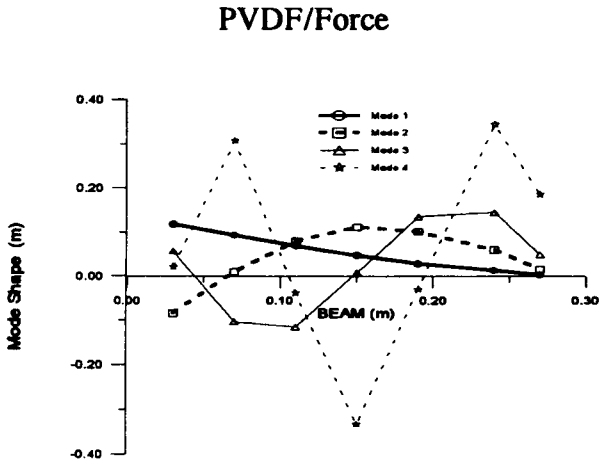

Figure 11. The prediction of the mode shapes from SMA for PVDF–Force.

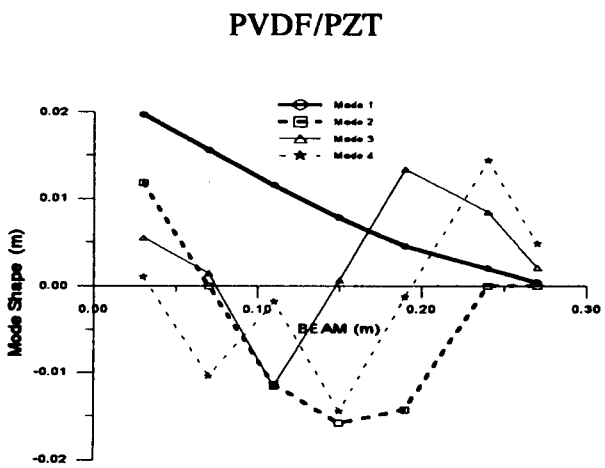

Figure 12. The prediction of the mode shapes from SMA for PVDF–PZT.

in figure 9, because only the even numbers of measuring points are considered for synthetic simulation. However, the nodal point positions and their shapes match very well with displacement mode shapes. The reason for obtaining the displacement mode shape for the accelerometer and PZT actuator pair is that the accelerometer is assumed to be roving during testing. A column of the FRF matrix is then obtained. The characteristics of the mode shapes are, therefore, determined by the mode shapes of the sensing device. As discussed previously, the accelerometer mode shape as shown in equation (30) is the displacement mode shape.

If the PVDF sensor is used as the output device, and the point force and PZT actuators are applied as the input devices, then the extracted mode shapes for both cases reveal the mirror image of the displacement mode shapes against the wall as shown in figures 11 and 12 respectively. The extracted mode shapes can also be characterized as the slope difference mode shapes for the cantilever beam. Because of the assumption that the PVDF sensor is roving instead of the actuator, the extracted mode shapes are dependent on the characteristics of the sensor mode shapes. One can expect that if the actuator is roving the actuator mode shape will be extracted. Therefore, the point force actuation will give the displacement mode shape, and the PZT actuation will result in the slope difference mode shape that is the mirror image of the displacement mode shape with a scaling factor $2\alpha_n \sin(\alpha_n l_c/2)$ against the wall for the cantilever beam. The relationship between the displacement and slope difference mode shapes is shown in the appendix.

5. Conclusions

This paper presents the use of accelerometers and PVDF sensors as sensing devices and point force and PZT actuators as actuation devices for a feasibility study of modal testing of a cantilever beam. Results show that the application of any combination of actuator and sensor to experimental modal testing can successfully determine the natural frequencies and damping ratio. The mode shapes can also be extracted and characterized as either displacement mode shapes or slope difference mode shapes depending on the types of transducer and modal testing procedures. Roving sensors will result in the sensor mode shapes, while roving actuators will result in the actuator mode shape. The mode shapes of both the accelerometer and the point force actuator that are the discrete types or point types of transducer are displacement essentially. The distributed types or strip types of piezoceramic transducer are shown to have the slope difference mode shape that is the mirror image of the displacement mode shape for the case of the cantilever beam. This work theoretically verifies the application of piezoceramic transducers to experimental modal testing of a cantilever beam. The idea of intelligent structural modal testing (ISMT) is withdrawn and can be incorporated with the use of an active controller to perform structural vibration and acoustic control. ISMT can be applied for fault diagnosis and also be extended for remote structural modal testing (RSMT).

Appendix. The relationship between the displacement and slope difference mode shapes

As discussed in subsection 2.4, point transducers will result in the displacement mode shapes, while piezoceramic transducers give the slope difference mode shapes between the two edges of the piezoceramic patches. The displacement mode shape is given by [26]

$$\phi_n(x) = \cosh\alpha_n x - \cos\alpha_n x - \sigma_n(\sinh\alpha_n x - \sin\alpha_n x) \quad \text{(A1)}$$

where

$$\sigma_n = \frac{\sinh\alpha_n L_b - \sin\alpha_n L_b}{\cosh\alpha_n L_b + \cos\alpha_n L_b}. \quad \text{(A2)}$$

The slope mode shape can be obtained by taking the first derivative of the displacement mode shape as follows

$$\phi_n'(x) = \alpha_n[\sinh\alpha_n x + \sin\alpha_n x - \sigma_n(\cosh\alpha_n x - \cos\alpha_n x)]. \quad \text{(A3)}$$

For the jth PZT actuator, the slope difference between the two edges of the PZT actuator can be obtained:

$$\phi_n^c(x_{c_j}) = \phi_n'(x_{c2_j}) - \phi_n'(n_{c_j}) = \phi_n'\left(x_{c_j} + \frac{l_c}{2}\right) - \phi_n'\left(x_j - \frac{l_c}{2}\right). \quad \text{(A4)}$$

By substituting equation (A3) into equation (A4), equation (A4) can be derived and expressed as follows:

$$\phi_n^c(x_{c_j}) = 2\alpha_n \sin\alpha_n \frac{l_c}{2}\left[\cosh\alpha_n x_{c_j}\frac{\sinh\alpha_n\frac{l_c}{2}}{\sin\alpha_n\frac{l_c}{2}} + \cos\alpha_n x_{c_j} - \sigma_n\left(\sinh\alpha_n x_{c_j}\frac{\sinh\alpha_n\frac{l_c}{2}}{\sin\alpha_n\frac{l_c}{2}} + \sin\alpha_n x_{c_j}\right)\right]. \quad \text{(A5)}$$

With the assumption of small length of piezoceramic patch, let l_c approach zero. One can obtain

$$\lim_{l_c\to 0}\frac{\sinh\alpha_n\frac{l_c}{2}}{\sin\alpha_n\frac{l_c}{2}} = 0. \quad \text{(A6)}$$

Therefore, equation (A5) can be simplified to

$$\phi_n^c(x_{c_j}) = 2\alpha_n \sin\alpha_n\frac{l_c}{2}[\cosh\alpha_n x_{c_j} + \cos\alpha_n x_{c_j} - \sigma_n(\sinh\alpha_n x_{c_j} + \sin\alpha_n x_{c_j})]. \quad \text{(A7)}$$

From equation (A1) for $x = x_{c_j}$,

$$\phi_n(x_{c_j}) = \cosh\alpha_n x_{c_j} - \cos\alpha_n x_{c_j} - \sigma_n(\sinh\alpha_n x_{c_j} - \sin\alpha_n x_{c_j}). \quad \text{(A8)}$$

Equation (A8) and the parenthesis in equation (A7) can be numerically demonstrated to be a mirror image pair. Therefore, the slope difference mode shape for the PZT actuator appears as the mirror image of the displacement mode shape with a scaling factor $2\alpha_n \sin(\alpha_n l_c/2)$. A similar derivation can also be obtained for the PVDF sensors.

References

[1] Han S and McConnell K G 1991 Analysis of frequency response functions affected by the coupled modes of the structure *Int. J. Anal. Exp. Modal Anal.* **6** 147–59

[2] Ebersbach P and Irretier H 1989 On the application of modal-parameter estimation using frequency-domain algorithms *Int. J. Anal. Exp. Modal Anal.* **4** 109–16

[3] El-Deeb K M M and Royles R 1992 Modal examination of an echinodome *Int. J. Anal. Exp. Modal Anal.* **7** 51–63

[4] Song S H and Koss L L 1993 Dynamic characteristics of an oil ball damper *Int. J. Anal. Exp. Modal Anal.* **8** 263–83

[5] Worden K, Wright J R, Al-Hadid M A and Mohammdd K S 1994 Experimental identification of multi degree-of-freedom nonlinear systems using restoring force methods *Int. J. Anal. Exp. Modal Anal.* **9** 35–55

[6] Wright J R and Al-Hadid M A 1991 Sensitivity of the force-state mapping approach to measurement errors *Int. J. Anal. Exp. Modal Anal.* **6** 89–103

[7] Sriram P, Craig J I and Hanagud S 1990 A scanning laser Doppler vibrometer for modal testing *Int. J. Anal. Exp. Modal Anal.* **5** 155–67

[8] Zhang P Q, Wang Q M, Wu X P and Huang T C 1992 Experimental modal analysis of miniature objects by optical measurement technique *Int. J. Anal. Exp. Modal Anal.* **7** 243–53

[9] Collins S A, Padilla C E, Notestine R J, von Flotow A H, Schmitz E and Ramey M 1992 Design, manufacture, and application to space robotics of distributed piezoelectric film sensors *J. Guidance Control* **15** 396–403

[10] Clark R L and Fuller C R 1992 Modal sensing of efficient acoustic radiators with PVDF distributed sensors in active structural acoustic approaches *J. Acoust. Soc. Am.* **91** 3321–9

[11] Wang B T 1994 Active control of far-field sound radiation by a beam: physical system analysis *Smart Mater. Struct.* **3** 476–84

[12] Young A J and Hansen C H 1994 Control of flexural vibration in a beam using a piezoceramic actuator and an angle stiffener *J. Intell. Mater. Syst. Struct.* **5** 536–49

[13] Crawley E F and de Luis J 1987 Use of piezoelectric actuators as elements of intelligent structures *AIAA J.* **25** 1373–85

[14] Clark R L, Fuller C R and Wicks A 1991 Characterization of multiple piezoelectric actuators for structural excitation *J. Acoust. Soc. Am.* **90** 346–57

[15] Wang B T and Rogers C A 1991 Laminate plate theory for spatially distributed induced strain actuators *J. Composite Mater.* **25** 433–52
[16] Wang B T and Rogers C A 1991 Modeling of finite-length spatially distributed induced strain actuators for laminate beams structures *J. Intell. Mater. Syst. Struct.* **2** 38–58
[17] Gibbs G P and Fuller C R 1992 Excitation of thin beams using asymmetric piezoelectric actuators *J. Acoust. Soc. Am.* **92** 3221–7
[18] Charette F, Guigou C, Berry A and Plantier G 1994 Asymmetric actuation and sensing of a beam using piezoelectric materials *J. Acoust. Soc. Am.* **96** 2272–83
[19] Bailey T and Hubbard J E 1986 Distributed piezoelectric-polymer active vibration control of a cantilevered beam *J. Guidance Control* **6** 605–11
[20] Clark R L, Burdisso R A and Fuller C R 1993 Design approaches for shaping polyvinylidene fluoride sensors in active structural acoustic control (ASAC) *J. Intell. Mater. Syst. Struct.* **4** 354–65
[21] Im S and Atluri S N 1989 Effects of a piezo-actuator on a finitely deformed beam subjected to general loading *AIAA J.* **27** 1801–7
[22] Dimitriadis E K, Fuller C R and Rogers C A 1991 Piezoelectric actuators for distributed vibration excitation of thin plate *J. Vib. Acoust.* **113** 100–7
[23] Lester H C and Lefebvre S 1993 Piezoelectric actuator models for active sound and vibration control of cylinders *J. Intell. Mater. Syst. Struct.* **4** 295–306
[24] Sun F P, Liang C and Rogers C A 1994 Experimental modal testing using piezoceramic patches as collocated sensor–actuators *Proc. 1994 SEM Spring Conf. and Exhibits* pp 871–9
[25] Cole D G, Saunders W R and Robertshaw H H 1994 The dynamic analysis of piezostructures in relation to modal analysis *Proc. 12th Int. Modal Anal. Conf.* pp 521–7
[26] Meirovitch L 1986 *Elements of Vibration Analysis* (New York: McGraw-Hill)
[27] Hubbard J E 1987 Distributed sensors and actuators for vibration control in elastic components *Noise-Con 87* pp 407–12
[28] Wang B T 1995 Characterization of transfer functions for piezoceramic and conventional transducers *ACTIVE-95* pp 805–16
[29] LMS 1993 *LMS CADA-PC User Manual*
[30] Piezo Systems 1990 *Product Catalog*
[31] Pennwalt Corporation 1990 *Piezo Film Sensor Application Notes*
[32] Wang B T and Wang C C Applications of piezoceramic actuators to experimental modal testing of cantilever beam *J. Technol.* at press (in Chinese)